



# In-process adaptive dimension correction strategy for laser aided additive manufacturing using laser line scanning

Peng Xu<sup>a</sup>, Xiling Yao<sup>b,\*</sup>, Lequn Chen<sup>b,c</sup>, Chenyang Zhao<sup>a</sup>, Kui Liu<sup>b</sup>, Seung Ki Moon<sup>c</sup>, Guijun Bi<sup>d,\*</sup>

<sup>a</sup> School of Mechanical Engineering and Automation, Harbin Institute of Technology, Shenzhen 518055, China

<sup>b</sup> Singapore Institute of Manufacturing Technology, Agency for Science, Technology and Research (A\*STAR), 73 Nanyang Drive, 637662, Singapore

<sup>c</sup> School of Mechanical and Aerospace Engineering, Nanyang Technological University, 50 Nanyang Avenue, 639798, Singapore

<sup>d</sup> Institute of Intelligent Manufacturing, Guangdong Academy of Sciences, Guangzhou 510070, China

## ARTICLE INFO

Associate Editor: Dr Jian Cao

### Keywords:

On-machine measurement  
Point cloud processing  
Tool-path generation  
Laser aided additive manufacturing  
Directed energy deposition  
Dimension correction

## ABSTRACT

Additive manufacturing (AM) technologies have seen rapid growth in the past decade. Achieving high-quality consistency and accuracy remains a challenge in the fabrication of large-format metallic parts using the directed energy deposition AM processes. An efficient dimension correction strategy is required to prevent build failure during the AM process. In this paper, a laser line scanning sensor was integrated into a robot-based laser aided additive manufacturing (LAAM) system to realise the on-machine measurement of the part geometry. With this system, an in-process adaptive dimension correction strategy was proposed. The dimensional deviations in the intermediate layers could be corrected immediately after they were detected during the LAAM process, thus avoiding excessive dimensional deviation leading to build failure. A tool-path generation process for dimension correction was proposed which did not rely on traditional time-consuming CAD reconstruction. Only 3D point cloud was used directly, enabling the quick response of the LAAM system in restoring the dimensional accuracy. The deviated surface could be automatically filled up, and the subsequent deposition processes were resumed after each cycle of the dimension correction. To facilitate the proposed dimension correction strategy, a Robot Operating System (ROS)-based software platform was developed. Experimental comparisons between the part built with and without correction were conducted. The results demonstrated a significant improvement in dimensional accuracy when the correction strategy was applied.

## 1. Introduction

Directed energy deposition (DED) techniques are suitable for large metal part fabrication, surface modification and repair. In the deposition process, either laser, electron beam, or arc melts metallic powders or wires can be used to form the desired part layer by layer. Schmidt et al. (2017) and Svetlizky et al. (2021) pointed out that many factors influenced the dimensional accuracy of the manufactured parts, such as powder/wire feeding rate, energy input, and printing speed. To produce high-quality products, various experimental approaches and numerical approaches, such as those presented by He et al. (2021) and Zhou et al. (2022), were used to obtain appropriate process parameters. Most commonly, the entire part is additively manufactured with pre-set constant process parameters and open-loop procedures from the beginning to the end. However, there is a complex interaction among the

laser beam, fed powder/wire and melt pool during the deposition process. Leach et al. (2019) found that undesirable physical phenomena (e.g., localised heat accumulation), as well as non-ideal process conditions (e.g., inconsistent printing speed), often deflect the process from the pre-optimised conditions, resulting in the loss of dimensional accuracy of the deposited components. As a result, dimensional accuracy is regarded as one of the major technical challenges that inhibit broader applications of DED. Early detection and correction of dimensional deviations are particularly important to enhance the part quality.

Increased efforts on process monitoring and process closed-loop control have been made to improve process stability and dimensional accuracy of the additively manufactured parts using DED. The process parameters, such as laser power, can be regulated in real-time based on various kinds of sensory feedback. Sensing deposition geometry, temperature, spectrum signals, and melt pool morphology has been the

\* Corresponding authors.

E-mail addresses: [yao\\_xiling@simtech.a-star.edu.sg](mailto:yao_xiling@simtech.a-star.edu.sg) (X. Yao), [gj.bi@giim.ac.cn](mailto:gj.bi@giim.ac.cn) (G. Bi).

<https://doi.org/10.1016/j.jmatprotec.2022.117544>

Received 11 December 2021; Received in revised form 18 February 2022; Accepted 26 February 2022

Available online 2 March 2022

0924-0136/© 2022 Elsevier B.V. All rights reserved.

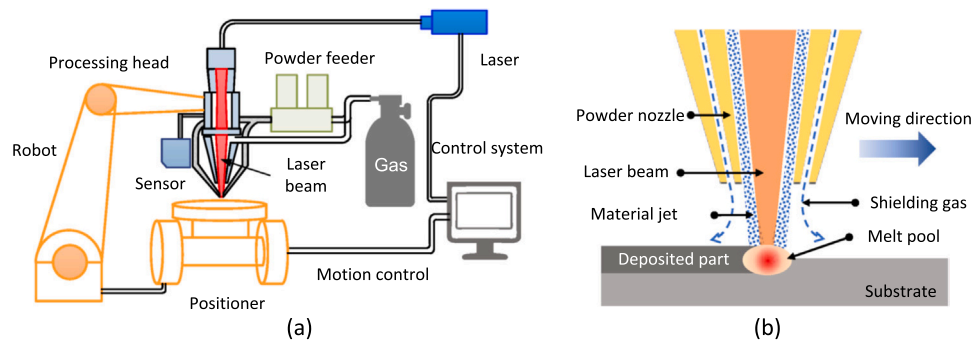


Fig. 1. (a) The schematic of the LAAM system, (b) Principle of the powder feeding and LAAM process.

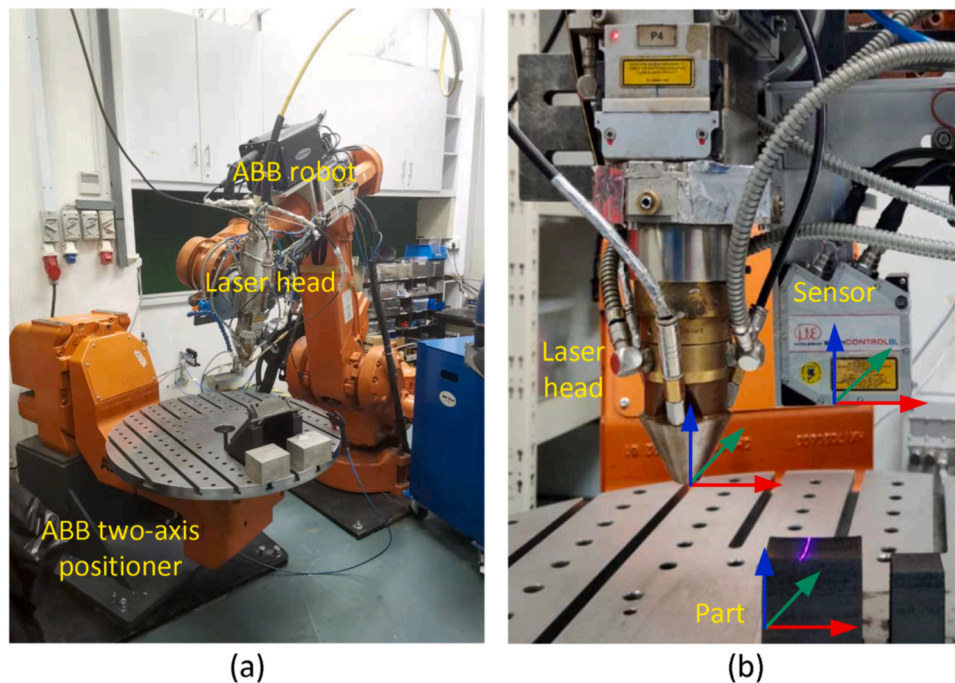


Fig. 2. (a) Setup of the robotic LAAM system, (b) coordinate frames of the laser head, sensor, and part.

focus. For example, Hofman et al. (2012) utilised a complementary metal-oxide-semiconductor (CMOS) camera to obtain the digital image of the melt pool. A method to extract the melt pool dimensions in real-time and a feedback control system was developed to adjust the laser power to compensate for the variations of the melt pool width. Gibson et al. (2020) used an in-axis thermal camera to measure the melt pool in real-time. A controller was created that modulates print speed and deposition rate on a per-layer basis. This allowed the control of average melt pool size alone or average laser power in conjunction with real-time melt pool size control. Lyu and Manoochehri (2021) integrated a 3D laser scanner to monitor online the geometric accuracy and the in-plane surface quality. The point cloud acquired from the laser scanner is processed and analysed using the Convolutional Neural Network to diagnose the anomalies. These results were used as feedback signals in the online control system to automatically adjust the process parameters for the Fused Filament Fabrication system. Akbari and Kovacevic (2019) used a CMOS camera to measure the width of the melt pool and then sent the data to an adaptive PI controller. Based on the error term that defined as the difference between the real-time melt pool width and its nominal value, the PI controller could adjust the laser power in response to variations in melt pool width. They were able to produce a consistent microstructure of the as-built part by applying this approach. Ding et al. (2016) used a similar method in which the powder flow rate was

controlled rather than the laser power.

The closed-loop control method shows its merit in suppressing local surface unevenness and promoting metallurgical homogeneity by improving the consistency of the system output value (e.g., melt pool size and temperature). However, there are several difficulties in this approach. Shi et al. (2020) showed that controller coefficients were mostly tuned through experiments involving human judgment, so they would not guarantee absolute avoidance of dimensional deviations. Jafari et al. (2021) showed the simultaneous control of multiple inputs remained a challenge in DED, although it was highly desirable since the dimensional inaccuracy was caused by the interaction of multiple sources of errors or instabilities. Additionally, Everton et al. (2016) found that the robustness of sensing signals was also key for implementing successful closed-loop control. As a result, when the DED process is not optimised for dimensional accuracy or the closed-loop controller fails to find the coefficients that completely prevent the dimension deviation, a more universal correction strategy is needed to correct such deviation regardless of its causation. The correction strategy should require no or minimal intrinsic parameter tuning.

In contrast to real-time monitoring and closed-loop control based on intra-layer melt pool signals, some recent works have shown another method for direct dimensional control with inter-layer measurement and correction. An in-process control strategy of build height was

**Table 1**  
LAAM process parameters.

Parameters	Value
Laser power	2.4 kW
Laser beam diameter	2 mm
Powder flow rate	7.7 g/min
Printing speed	20 mm/sec
Hatch spacing	1 mm
Layer thickness	0.5 mm

presented by Garmendia et al., (2018, 2019). After each interval that contained a fixed number of layers, the deposition was suspended, and the actual build height was measured with a structured light scanner. The number of layers to deposit in the next interval was recalculated based on the theoretical layer height to ensure that the correct build height could be achieved. Kono et al. (2020) proposed an in-process layer height updating strategy based on the measurement of the part height. However, the height of the layer was determined by the mean value of the measured surface. Only the error of the average layer height was considered during the dimension control. In actual DED applications, the surface topography should also be considered to ensure dimensional accuracy. Each deposited layer acts as the substrate of the next layer. As a result, areal surface topography errors can be propagated and accumulated with the deposition, leading to an irreversible geometric non-conformance even when the average layer height is correct.

Therefore, this paper proposed a novel methodology for in-process dimension correction based on on-machine laser scanning measurements in the laser aided additive manufacturing (LAAM) which uses a laser beam for powder-blown/wire-fed deposition process. The main contribution is the development of a point cloud-based dimension correction strategy that eliminates the dimensional deviations in-process through updating the deposition tool-path. The generation of the correction tool-path does not rely on computationally expensive computer-aided design (CAD) reconstruction. Only 3D point cloud data is directly used for computing the correction tool-path. The proposed

point cloud-based method enables the correction to be done in-process and autonomously. It is more efficient than traditional CAD-based tool-path planning methods requiring offline CAD reconstruction and alignment with manual operation on specialized software. Another advantage is that dimensional deviations in the intermediate layers can be corrected at the early stage (immediately after they are detected) to prevent further distortions, while traditional CAD-based methods perform correction only in the out-most layers. Experimental validation was carried out with a robot-based LAAM system and on-machine measurement. The results showed that the dimension correction strategy was effective and would not jeopardise the mechanical quality of the part.

## 2. Methodology

### 2.1. Experimental setup

The schematic and the photo of the LAAM system are illustrated in Fig. 1 and Fig. 2. The system integrated a coaxial powder feeding nozzle and a laser head with a six-axis articulated robot (ABB IRB 4400). A two-axis positioner (ABB IRBP A) was used to hold the workpiece. The robot and the positioner can be synchronised and controlled by an ABB IRC5 controller to move the laser head along the target tool-paths. The laser source was a 1070 nm Ytterbium fiber laser system (IPG YLS-6000) with 6 kW maximum power. A GTV powder feeder delivered metallic powders to the powder feeding nozzle with pure Argon as the carrier and shielding gas. The LAAM process parameters were listed in Table 1 and the used powder material was Inconel 718. The standoff distance between the nozzle tip and the substrate was set as 12 mm.

### 2.2. On-machine laser scanning measurement

In this work, on-machine measurement was achieved for quality inspection without having to remove the workpiece from the manufacturing system. As shown in Fig. 2, a laser displacement sensor (Micro-Epsilon ScanCONTROL 2950-50/BL) was chosen as the surface topography measuring sensor and was mounted on the robot next to the

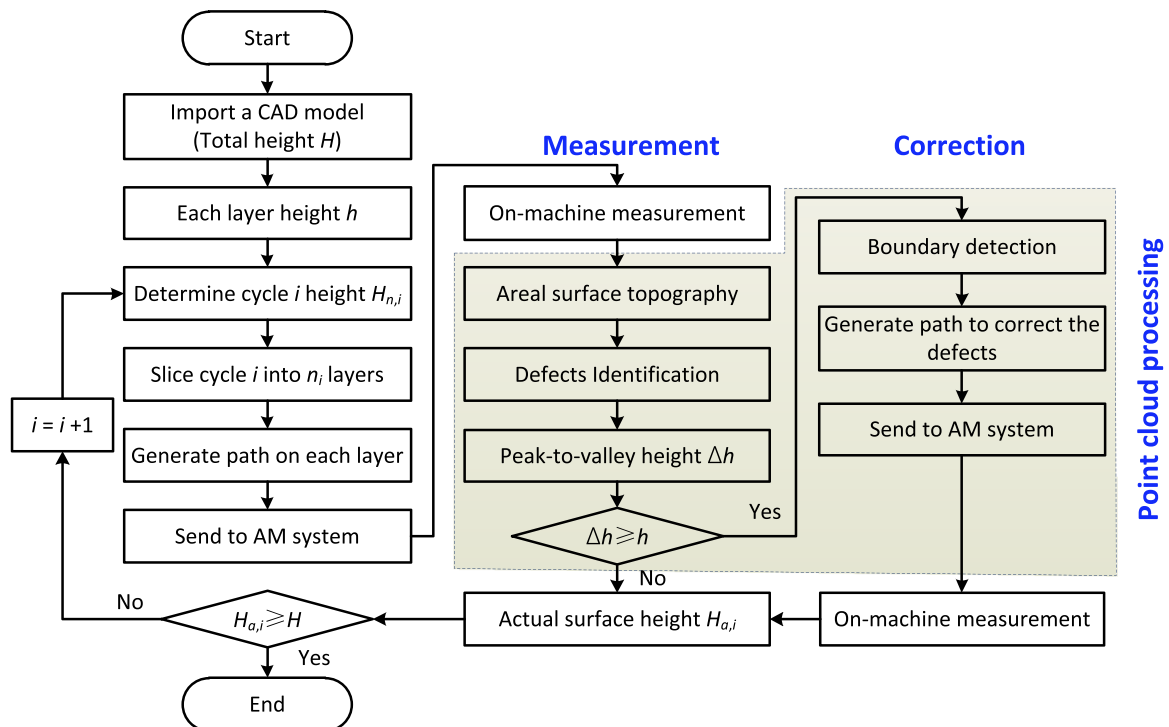


Fig. 3. Flowchart of the proposed in-process adaptive dimension correction strategy.

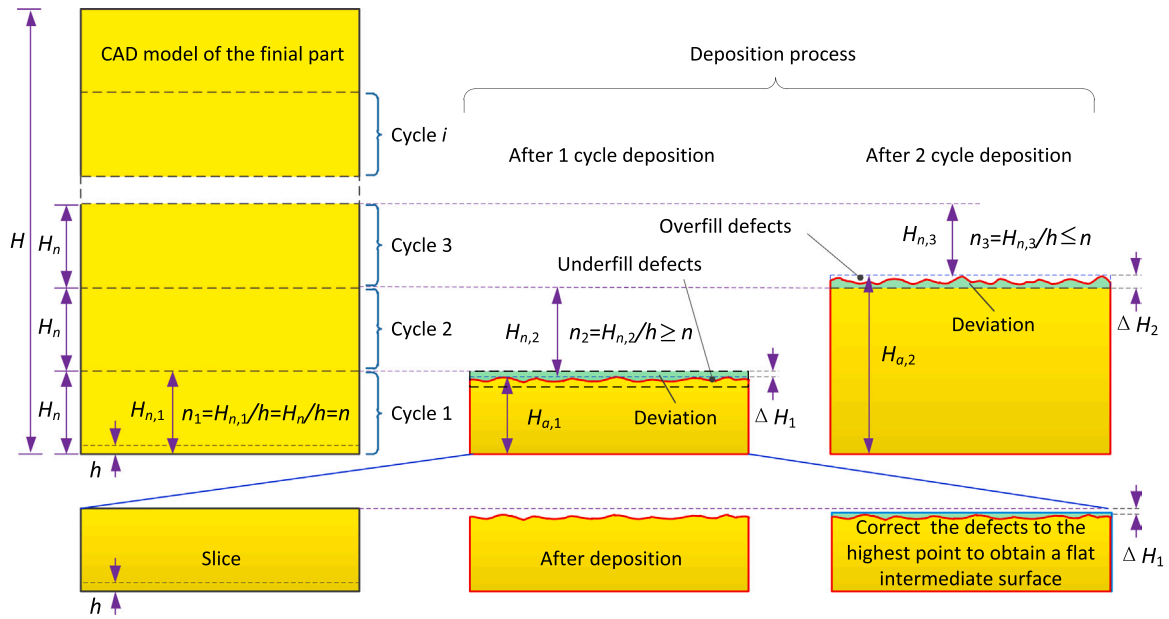


Fig. 4. Illustration of the proposed in-process adaptive dimension correction strategy.

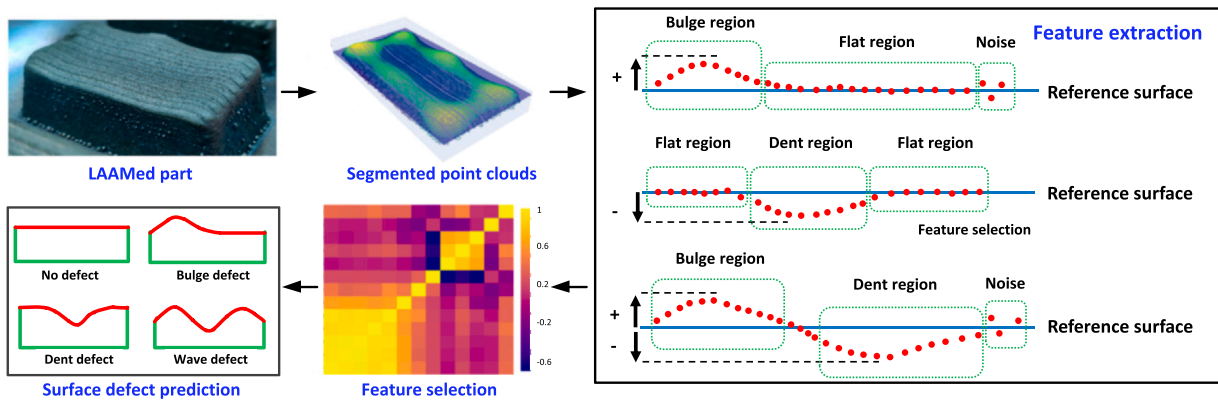


Fig. 5. Rapid surface defect identification with in-situ point cloud processing and machine learning.

laser head. The reference resolution in Z-axis is 4 μm. The laser displacement sensor was built on the concept of the laser triangulation principle (Ding et al., 2021; Li et al., 2020). To obtain the accurate position of the sensor relative to the laser head, hand-eye calibration of the laser displacement sensor was conducted using the method presented by Li et al. (2021). Based on the principle of triangulation measuring, the laser displacement sensor could obtain surface topography of the manufactured part represented by the 3D point cloud in the sensor coordinate system. Then, the point cloud in the robot coordinate system could be expressed as

$$\begin{bmatrix} p_R \\ 1 \end{bmatrix} = \begin{bmatrix} R_R^E & T_R^E \\ \mathbf{0} & 1 \end{bmatrix} \begin{bmatrix} R_E^S & T_E^S \\ \mathbf{0} & 1 \end{bmatrix} \begin{bmatrix} p_S \\ 1 \end{bmatrix} \quad (1)$$

where  $p_R$  and  $p_S$  are the surface point data in the robot and sensor coordinate system,  $R_E^S$  and  $T_E^S$  are the sensor's rotation matrix and translation vector with respect to the robot end-effector identified by the hand-eye calibration, the pose of robot end-effector  $R_R^E$  and  $T_R^E$  is known as it is directly controllable.

The part was scanned with a speed of 20 mm/s, at 90 mm above the part's surface. Each laser scan line contained 640 measurement points. The raw point cloud contained noise. After removing the noisy points, the top surface of the part can be extracted. The details of point cloud

filtering, surface extraction and surface defect identification process were demonstrated in our previous work (Chen et al., 2021).

### 2.3. Dimension correction strategy

This section provides an overview of the proposed in-process adaptive dimension correction strategy during the LAAM process. The flowchart of the proposed in-process adaptive dimension correction strategy is shown in Fig. 3. The illustration of the proposed strategy is shown in Fig. 4. Following this, a dedicated software toolchain was developed, which consisted of the following key procedures.

First of all, CAD model of the part was created. To extract the cross-sectional boundaries of the geometry at a given height, a direct slicing algorithm of the CAD file was applied. The entire model was sliced in multiple cycles with  $H_n$  being predefined by the end-user. For the  $i$ -th cycle, a portion of the CAD model with a height  $H_{n,i}$  was picked.  $H_n$  and  $H_{n,i}$  might be slightly different due to the surface deviation in the previous cycle. By slicing the selected model from bottom to top with layer height  $h$ , a group of 2D layers  $n_i$  ( $n_i = H_{n,i}/h$ ) was obtained, which represented the cross-sectional geometry of the part.

Secondly, deposition tool-paths were generated on each layer to guide the laser head to fill the boundary and interior. Constant parameters (e.g., the printing speed and hatch spacing) were pre-set in the tool-

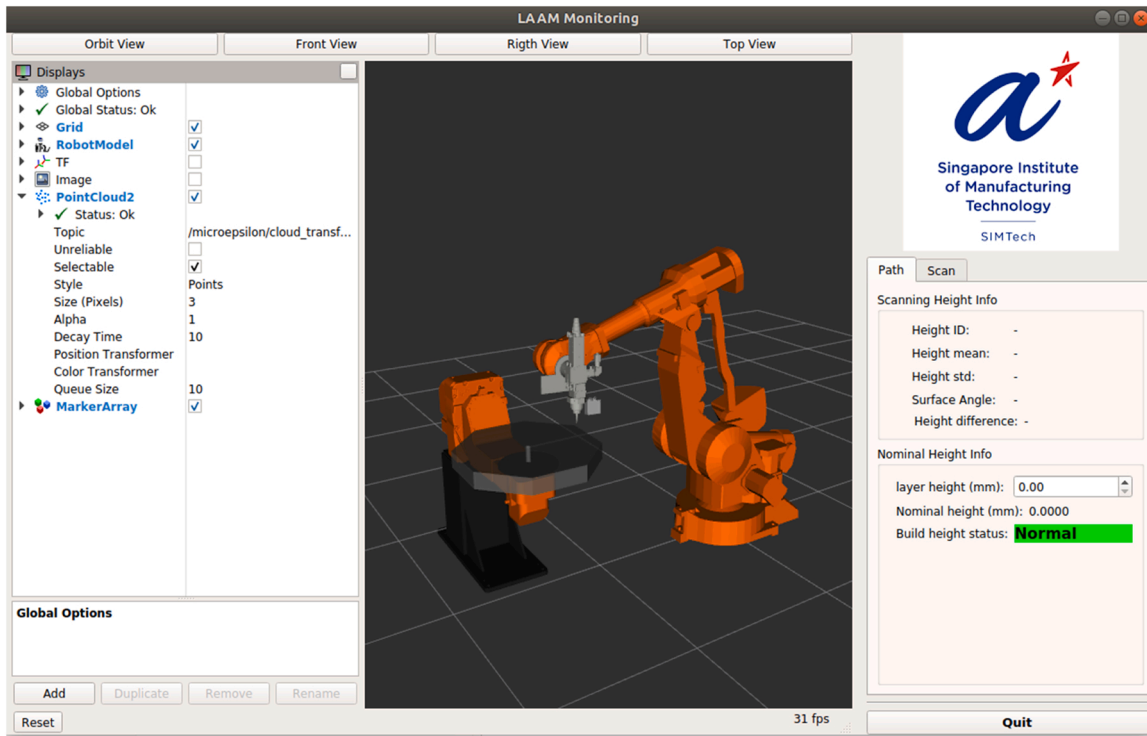


Fig. 6. Graphical interface of the developed software platform based on RViz.

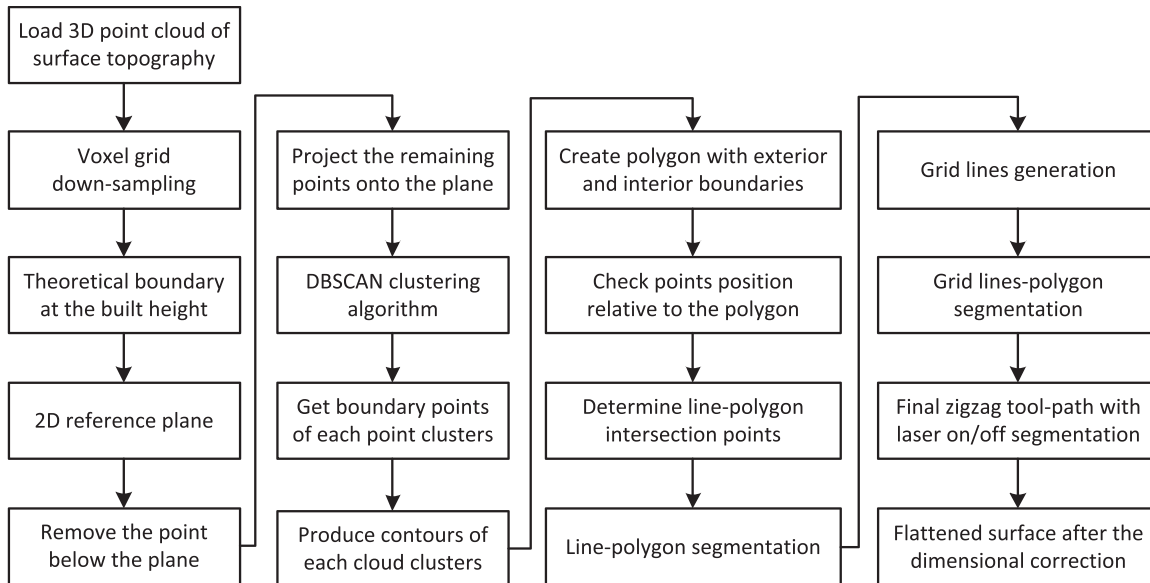


Fig. 7. Function execution flowchart for point cloud processing and correction tool-path generation.

paths. Once the tool-paths were generated, they were converted into the robot control program, and sent to the LAAM system. The selected portion of the part was deposited.

Thirdly, the LAAM process was suspended once the deposition was finished in the current cycle. The intermediate surface was measured by the laser displacement sensor to obtain the surface topography of the actual part. The surface defects were identified using an in-house developed algorithm after processing and analysing the acquired 3D point cloud data, which was presented in our previous work (Chen et al., 2021). As depicted in Fig. 5, the surface defect identification approach involves in-situ point cloud processing with machine learning feature extraction and online defect prediction. The decision was then made on

whether the defects should be corrected to avoid further deterioration of the accuracy. If the peak-to-valley height of the surface defect  $\Delta h$  was higher than one layer height  $h$ , correction was required, and the correct action would be taken in the fourth step. Otherwise, no correction was required and the fifth step below was executed.

Fourthly, the point cloud boundary at a certain height of the deviations was detected, and the tool-paths for correction were generated. For both concave and convex regions, the defects were filled up to the highest point to obtain a flat surface. Unlike conventional tool-path generators that required an input CAD model, the correction tool-path was created directly from the point cloud data, which was a key advantage since the computationally expensive CAD reconstruction step

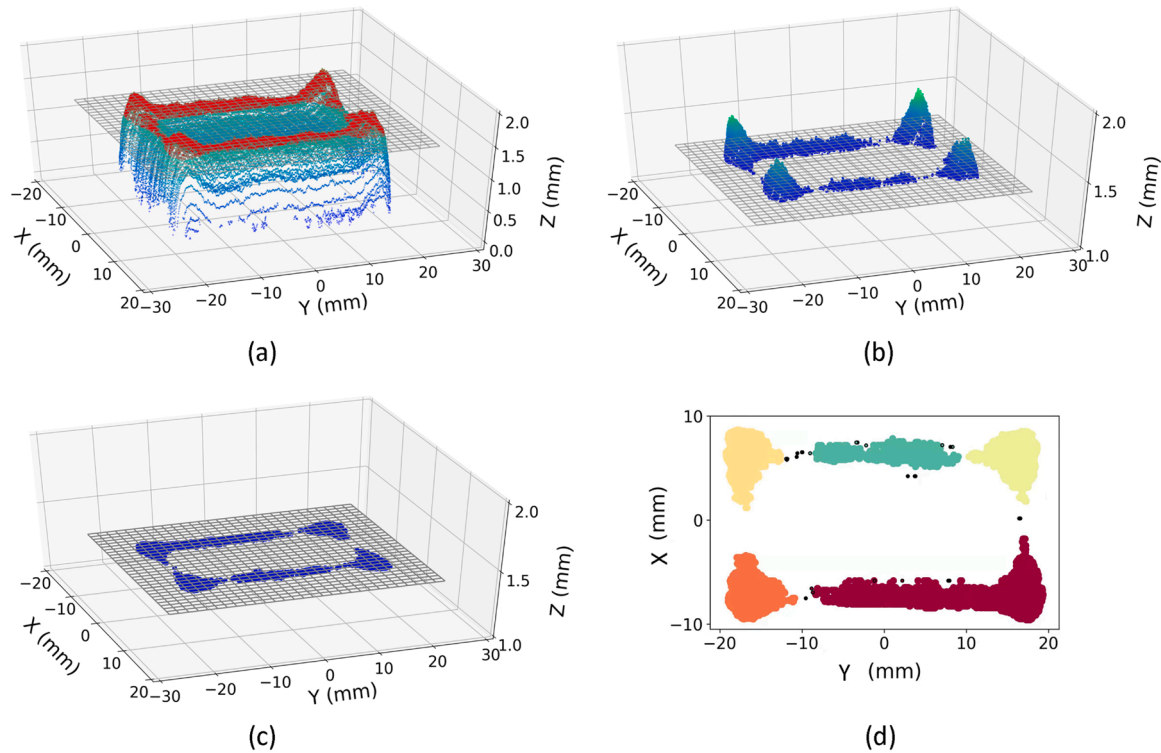


**Fig. 8.** Point cloud processing: (a) visualisation of 3D point clouds and 2D reference plane, (b) points below the reference plane were removed, (c) remaining 3D point clouds projected onto the reference plane, and (d) clustering result showing five different point cloud clusters.

was eliminated. Once the correction tool-paths were generated, they were converted into the robot control program and executed by the LAAM system. More details regarding the correction tool-path generation method will be given in Section 4.

Fifthly, a flat surface was obtained with the actual height  $H_{a,i}$  in the  $i$ -th cycle. However, there may still be a build height deviation  $\Delta H_i$  from the prescribed value ( $\Delta H_i = iH_n - H_{a,i}$ ). When this happened, the number of the deposited layers ( $n_{i+1}$ ) in the next cycle was recalculated and updated in the robot control program. By using the strategy of recursive measuring and redefining the tool-path, the dimensional accuracy of the final part was ensured. Each cycle, the aforementioned five processes were repeated to deposit a different section of the component until the entire part was completed.

A software platform with a graphical interface was developed in-house to facilitate the proposed dimension correction strategy. Inspired by the work in (García-Díaz et al., 2018), the open-source Robot Operating System (ROS) was employed to establish sensor-robot communication. The software allowed the logging and visualisation of the point cloud data, and it synchronised the sensor capturing, robot motion, and laser operation based on the procedures in the dimension correction strategy. A snapshot of the ROS-based software platform is shown in Fig. 6, highlighting a digital twin of the robotic LAAM system shown in RViz, the 3D visualizer for ROS, which can reflect the robot physical movement and sensor measurement result in real-time.

### 3. Point cloud processing and correction tool-path generation

In this section, a point cloud processing and correction tool-path generation algorithm was proposed. The development of the automatic correction tool-path generation algorithm is one of the key contributions of this work. The flowchart in Fig. 7 illustrates the procedure of the dimension correction process, and the details of each step are explained as follows.

The 3D point cloud of the part surface after noise filtering and in-situ processing, which was given by Chen et al. (2020), was loaded into the

in-house developed software platform. 3D voxel grid down-sampling method (Han et al., 2017) was used to reduce the total number of points. In each voxel (a small cubical volume in the 3D space), the centroid was used to approximate all the points lying within the voxel, thereby reducing the point cloud size for faster computations. Fig. 8 visualises the point cloud processing steps. It shows the measured 3D point cloud of a part's surface with significant dimensional deviation in the workpiece coordinate frame. Excessive material and geometric distortions can be found at the edges and corners of the part. The distortions were generated by the build-up of residual thermal stress during the deposition, which caused thermal contraction and expansion. The fast melting and cooling cycles, as well as the dynamic interplay between the process parameters, make real-time control challenging. In this instance, in-process dimension correction is required to avoid further surface quality degradation or build failure. In order to generate the correction tool-path, a critical step was to extract the deviation boundary from the point cloud. The nominal cross-sectional area was represented as the 2D reference frame shown in Fig. 8(a). The measured 3D point cloud was sliced by the reference plane, as shown in Fig. 8(b), where the points below the reference plane were removed. Then, the remaining point clouds were projected onto the 2D reference frame, as shown in Fig. 8(c). Subsequently, the DBSCAN clustering algorithm presented by Ester et al. (1996) was applied to segment the projected 2D point cloud into multiple groups. In the DBSCAN clustering, points were clustered based on their density and occupying space. In Fig. 8(d), point clouds were clustered into five groups. The black dots represent noisy points that do not belong to any clusters as their distance is too far from their neighbours.

After the point cloud clustering step, the contours of each cluster need to be identified, which defines the deviation boundary for bulge surface defects. There are many bounding hull algorithms in the literature, such as concave hull presented by Moreira and Santos (2007), alpha-shape presented by Edelsbrunner et al. (1983), and alpha-concave hull presented by Asaeedi et al. (2017). Due to its flexibility in dealing with an arbitrary set of points, the concave hull algorithm was used in

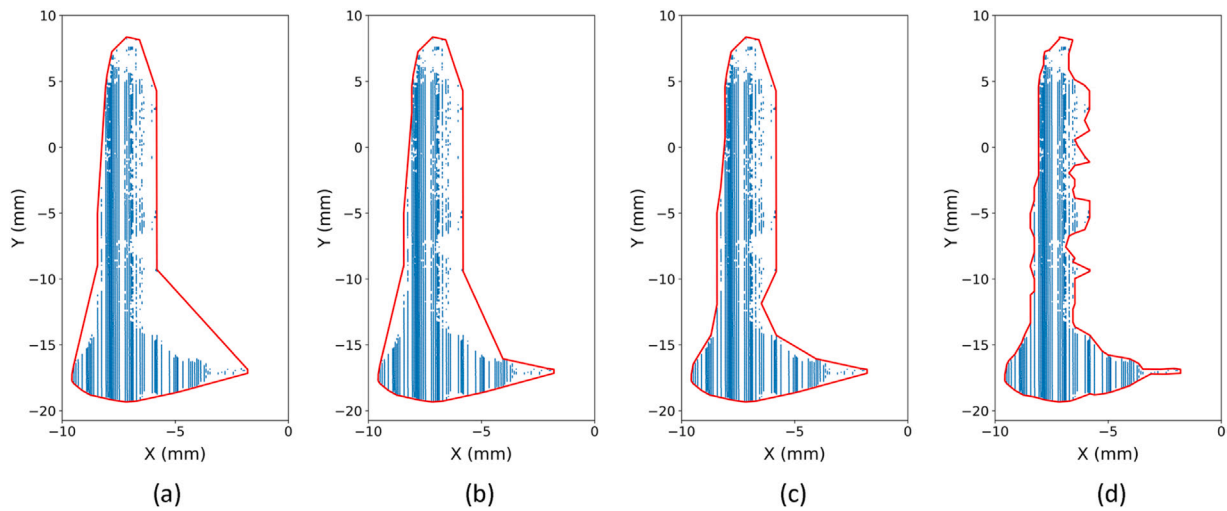


Fig. 9. The concaveness/smoothness of the bounding polygon with different tolerances: (a)  $\delta = 10$ , (b)  $\delta = 8$ , (c)  $\delta = 4$ , and (d)  $\delta = 1$ .

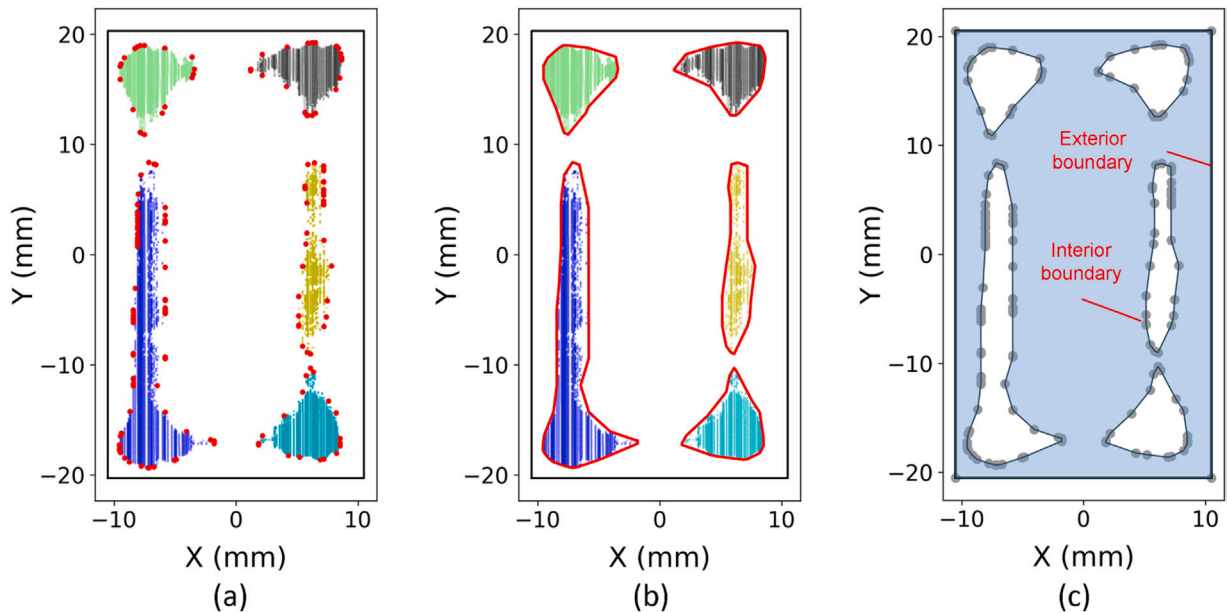


Fig. 10. Polygon generation process: (a) clustered point clouds with boundary points (in red colour) and the rectangular theoretical cross-section, (b) the boundary polygons of each point cloud cluster (in red colour), and (c) the deposition polygon (in blue colour) with exterior (theoretical) and interior boundaries.

this study, with a few modifications to increase its computational efficiency. The concave hull algorithm is described by the pseudocode in Appendix A. The tolerance  $\delta$  controlled the concaveness of the computed hull. The algorithm found the boundary points of the concave polygon iteratively, and the computational time was less than 1 s for over two thousand points. The concave hull generation process started with determining the convex boundary. Firstly, the Delaunay triangulation (DT) algorithm presented by Lee and Schachter (1980) was applied to generate triangle meshes among the points. For a triangulation to be valid, it must not have duplicate points, triangles formed from colinear points, or overlapping triangles. The DT algorithm built triangle grids by propagating triangles from a random starting position to the point cloud's edge. In the DT algorithm proposed by Guibas and Stolfi (1985), no other points were allowed to be within a triangle's circumcircle. Eventually, each triangle was formed by the three nearest points without intersection segments. As a result, a convex polygon hull was formed by the outermost boundary of the triangular mesh.

After applying the DT algorithm, the triangles at the outermost

boundary were selectively deleted based on the tolerance  $\delta$ . Boundary edges larger than  $\delta$  were added to the deletion list. Triangles that contained more than one boundary edge were not deleted. As a result, the concave hull was a reduced form of the original convex hull. Fig. 9 shows the bounding polygon for a point cloud cluster with different  $\delta$  values, indicating that a smaller  $\delta$  results in a finer concave hull.

Considering the smoothness and accuracy of the boundary,  $\delta = 4$  was chosen in this study. The result of the concave boundary points identification of each point cloud cluster is shown in Fig. 10(a). As each point cloud cluster represented the over-built bulge area with excessively deposited materials, the dimension correction process must avoid depositing materials onto those regions. For each cluster, a closed contour polygon was generated by connecting the boundary points, as shown in Fig. 10(b). The bounding polygons were termed as interior boundaries. The theoretical boundary was also extracted from the CAD model at the same height as the built boundary. To correct the dimensional deviations, materials should only be deposited at the region between the theoretical and interior boundaries, as depicted by the region

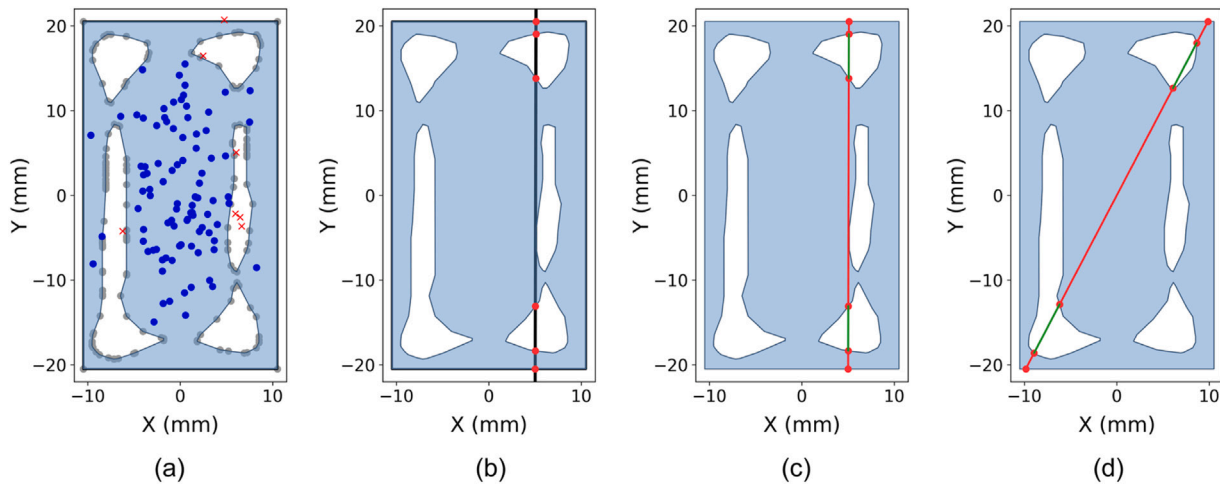


**Fig. 11.** Illustration of tool-path segmentation process: (a) points' position relative to the polygon, (b) line-polygon intersection points represented as red dots, (c) straight line-polygon segmentation result, and (d) oblique line-polygon segmentation result.

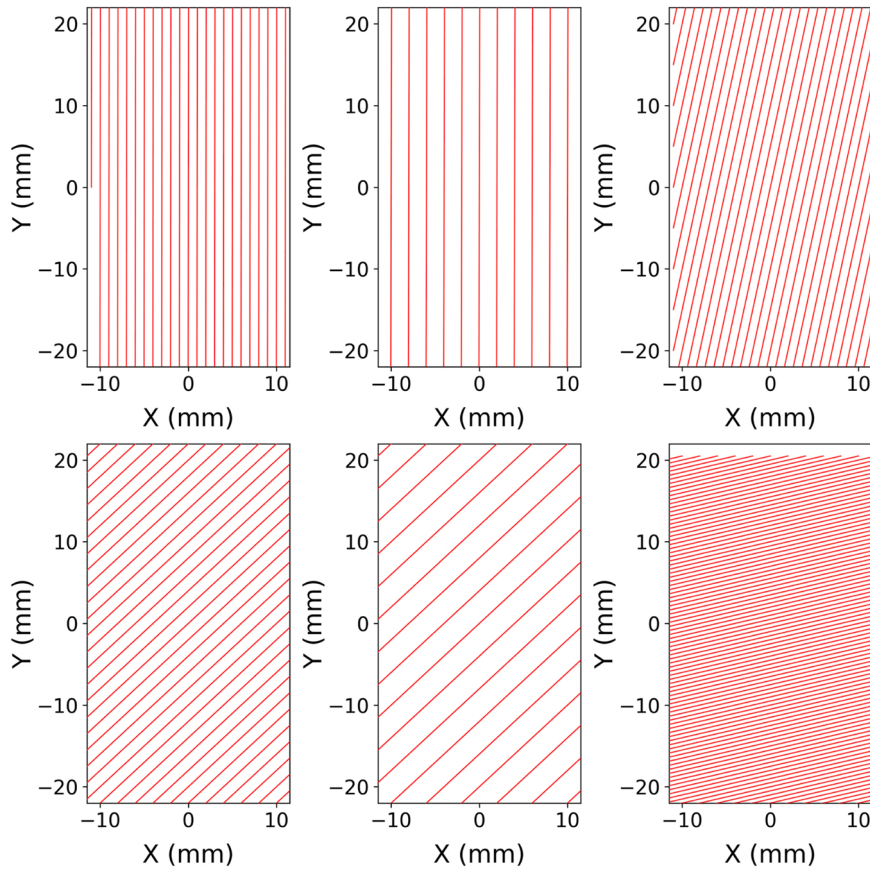


**Fig. 12.** Zigzag tool-path grid line generation with various deposition patterns.

in Fig. 10(c). The deposition region was the dent surface in blue colour represented by a polygon with exterior (theoretical) and interior boundary lines. The laser was turned off to avoid melting excessive material if it was inside the interior boundaries. The laser was turned on only if it is inside the blue deposition region so that it could melt and deposit metallic material to fill up the dent surface. The nominal process parameters (e.g., laser power, scanning speed, powder feeding rate, etc) along the correction tool-path were the same as those in the last deposition cycle to ensure the consistency in material properties before and after the dimension correction. For dimensional deviations larger than

the nominal layer height, multiple layers of correction tool-path were generated so that the corrected part could have a flat surface at the end of the current deposition cycle.

The tool-path segmentation process is performed to generate the correction tool-path with laser on/off segments, as illustrated by Fig. 11. Firstly, the points' positions relative to the polygon were determined, as shown in Fig. 11(a). Some random points were generated to test if they were outside or inside the polygon boundaries. The red crosses represent positions lying outside polygon or inside holes (interior boundaries), and the blue dots represent positions lying within the deposition region

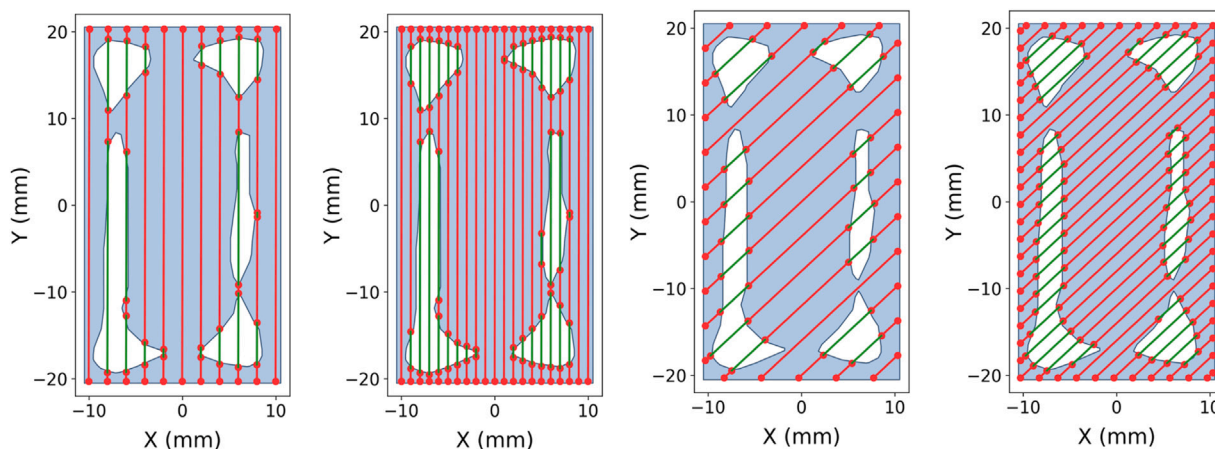


Fig. 13. Final zigzag tool-path generation results with different deposition patterns, where green lines represent laser-off segments, and red lines represent laser-on segments.

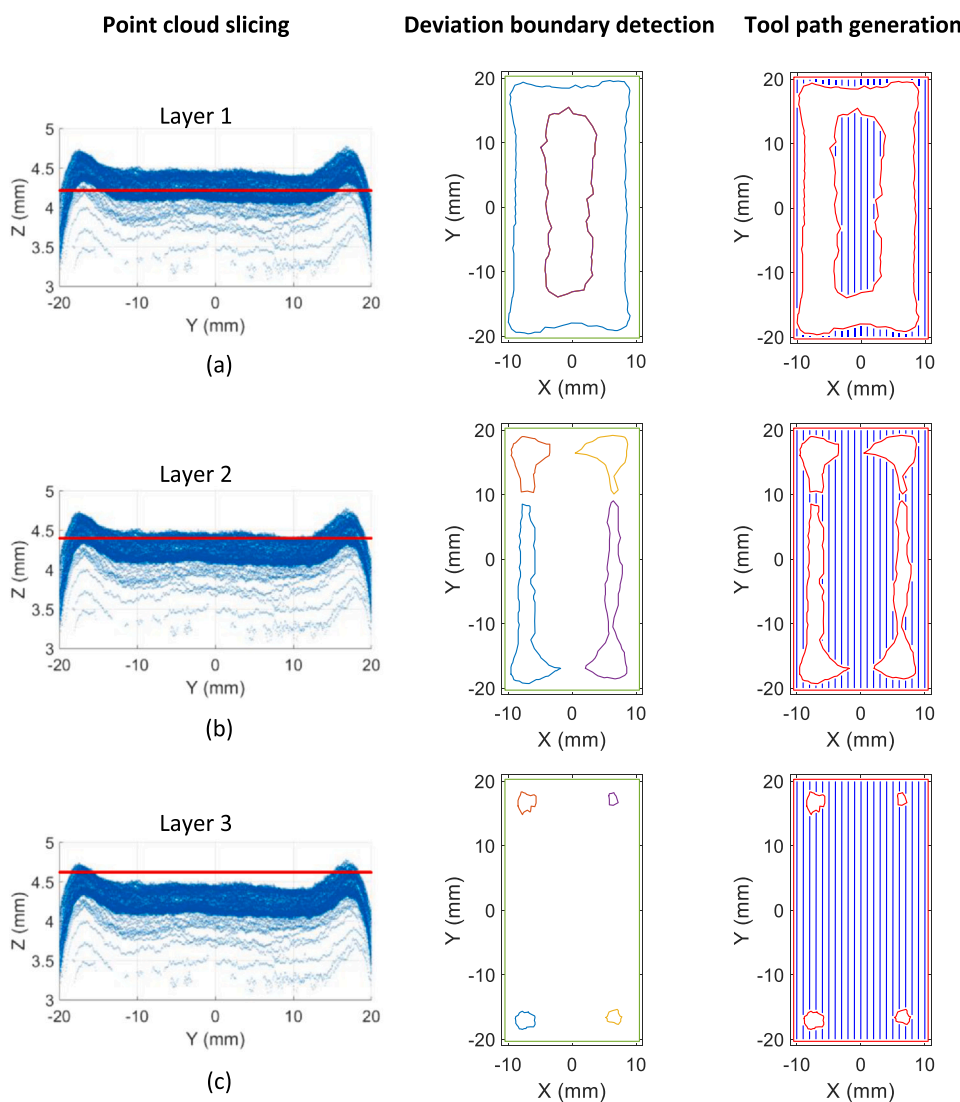


Fig. 14. Point cloud processing and correction tool-path generation for three sliced layers.

of the polygon. Then, the line-polygon intersection points were found, as depicted by the red dots in Fig. 11(b). Lastly, the line was segmented by the polygon, where portions lying within the blue deposition region

corresponded to the laser-on segments, and portions lying within the interior boundaries were laser-off segments. The line-polygon intersection and segmentation algorithms are described by the pseudocode in

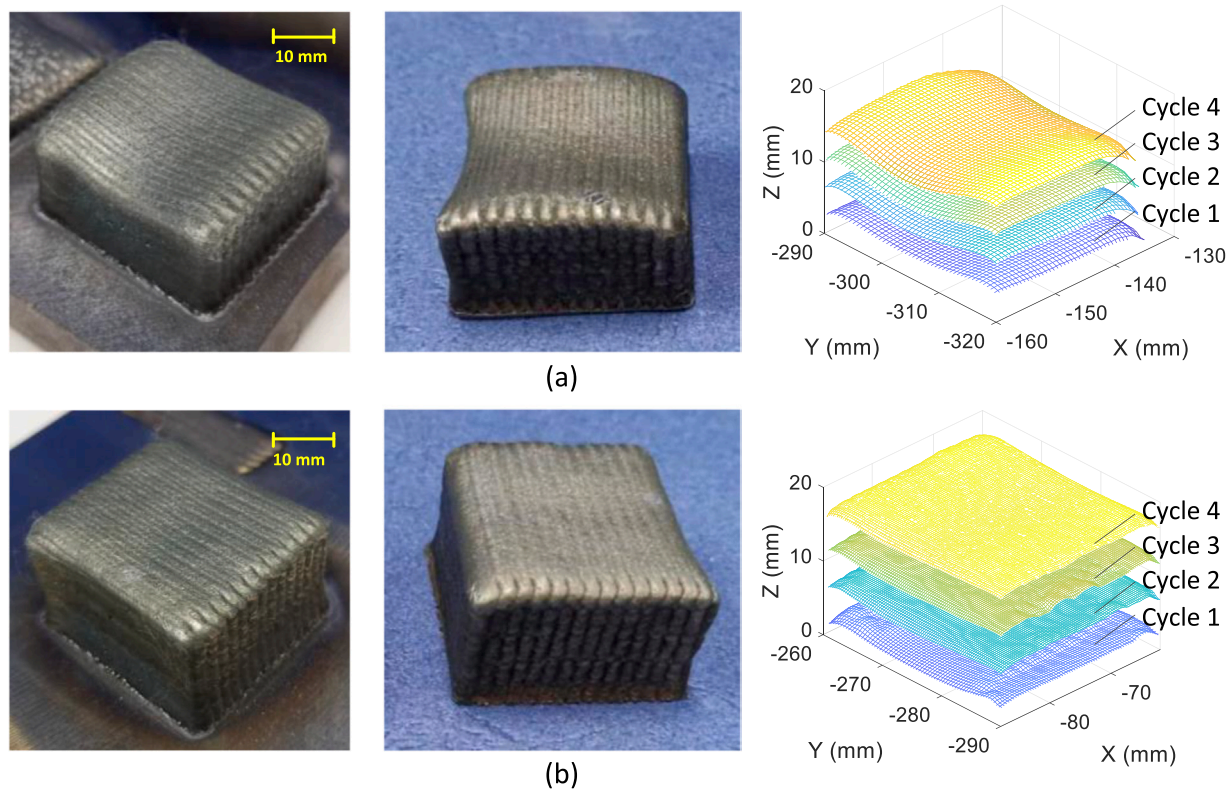


Fig. 15. Comparison of the LAAM-fabricated parts: (a) without correction; and (b) with correction.

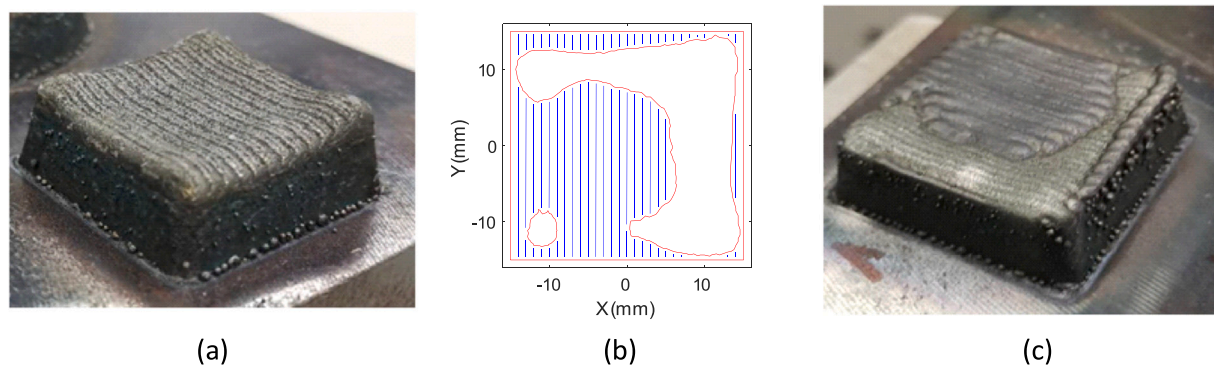


Fig. 16. Point cloud-based tool-path generation and dimension correction for one sliced layer: (a) original part with severe geometric distortions, (b) generated correction tool-path (laser-on segments), and (c) part after one layer of dimension correction.

Appendix B. Essentially, the algorithm iterated through all the polygon's exterior and interior boundary edges to find the intersection points and store them. The algorithm subsequently divided the line into laser-on segment and laser-off segment according to the points' position relative to the polygon. The results of line-polygon segmentation are illustrated in Fig. 11(c) and (d). It can be seen that lines with arbitrary orientations could be segmented by the proposed method easily. Green segments are in holes and red segments are in the polygon. The intersection points are the position to initiate the laser on/off signals.

Fig. 12 shows the generation of zigzag tool-path grid lines with various deposition patterns. The pattern is controlled by three parameters  $\Delta x$ ,  $\Delta y$  and  $nl$ . Parameter  $\Delta x$  specifies the interval of lines in the X-direction, while  $\Delta x/\Delta y$  determines the slope of the lines. A larger  $\Delta y$  means lines are closer to 90 degrees relative to the X-direction. When  $\Delta x/\Delta y$  equals 1, the slope of the line is equal to 45 degrees. The parameter  $nl$  controls the size of the grid lines. Fig. 13 demonstrates the final zigzag tool-path generation results, with various possible

deposition patterns. The green lines represent laser-off segments, and the red lines represent laser-on segments. All the tool-paths are segmented successfully by the algorithm regardless of their orientation or track width.

Fig. 14 shows an overview of the point cloud processing and correction tool-path generation. As the depth of the dent surface defect was larger than the nominal layer height in this example, multiple layers of correction tool-paths were generated to fill up the dent regions, which enables the part to have a flat surface at the end of correction. The point cloud was sliced by the reference plane into three layers based on the nominal layer height. Then the deviation boundaries were extracted, and the tool-path for each correction layer was generated with laser-on and laser-off segments.

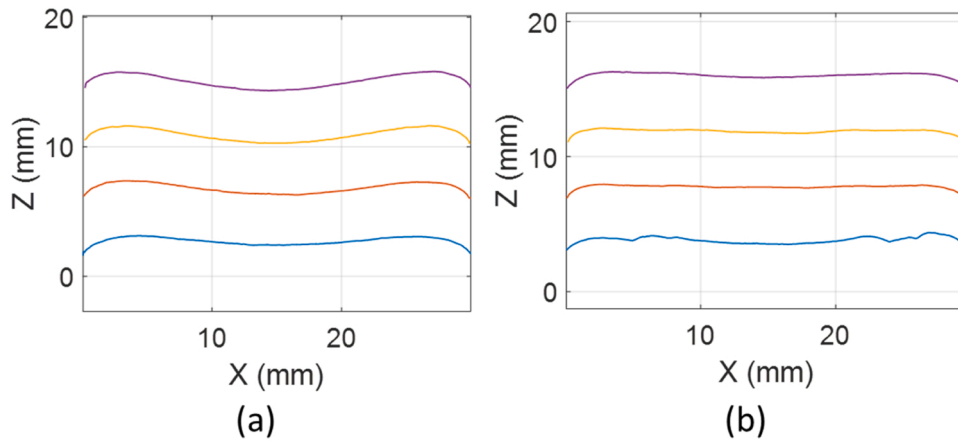


Fig. 17. Growth of the part: (a) without correction, and (b) with correction.

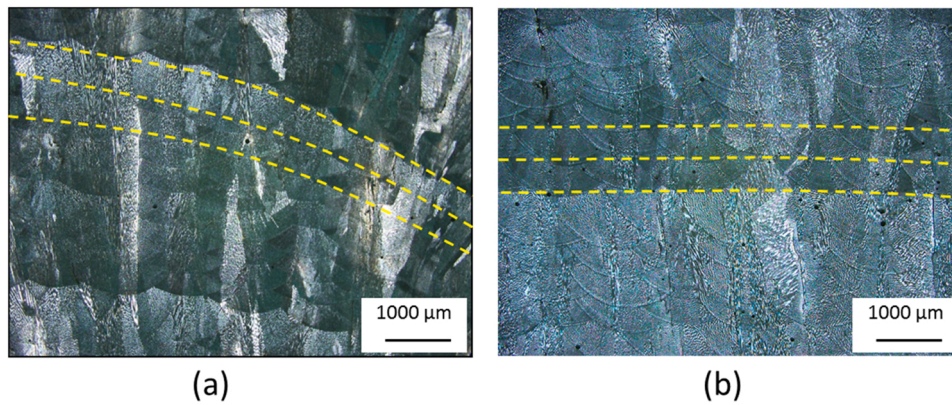


Fig. 18. Cross-sections of the as-deposited parts in the XZ-plane: (a) without correction, (b) with correction.

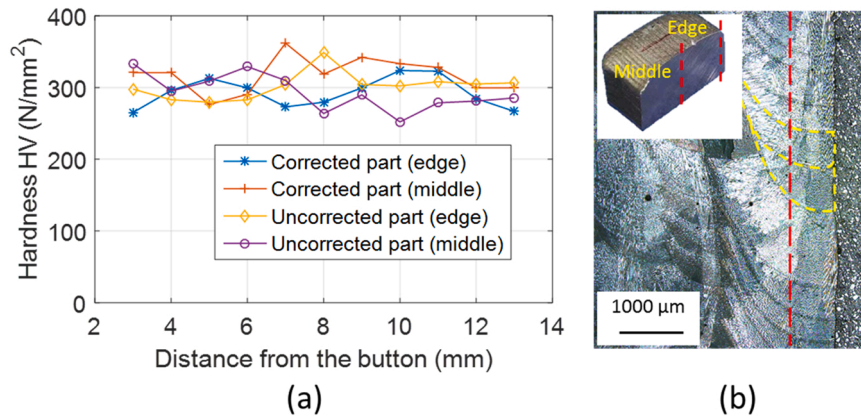


Fig. 19. (a) Hardness profiles, (b) the cross-section showing the edge and middle lines where the hardness tests are conducted.

#### 4. Results and discussion

##### 4.1. Dimensional accuracy enhancement

Experiments were conducted to validate the effectiveness of the proposed method. The theoretical CAD model was a rectangular block with 30 mm in both length and width, and 16 mm in height. Dimensional deviations were inevitable even with optimised tool-paths, as the LAAM process becomes unstable over time due to heat accumulation at the edges. In this experiment, the tool-path was not optimised for the chosen geometry and material, and hence significant dimensional

deviation was expected to occur within the first few layers. Two solid parts were manufactured, the first one was built continuously without dimension correction, and the second one was built with the proposed dimension correction strategy implemented. The comparisons between the two parts are shown in Fig. 15.

For each part, 32 layers were deposited using the same process parameters. On-machine laser scanning measurements were conducted at every cycles during the deposition process (i.e., at layer 8, layer 16, layer 24 and layer 32, respectively). For the uncorrected part, a saddle-shaped deviation occurred, as shown in Fig. 15(a). This was caused by the instantaneous decrease of the robot speed at the start and the end of the

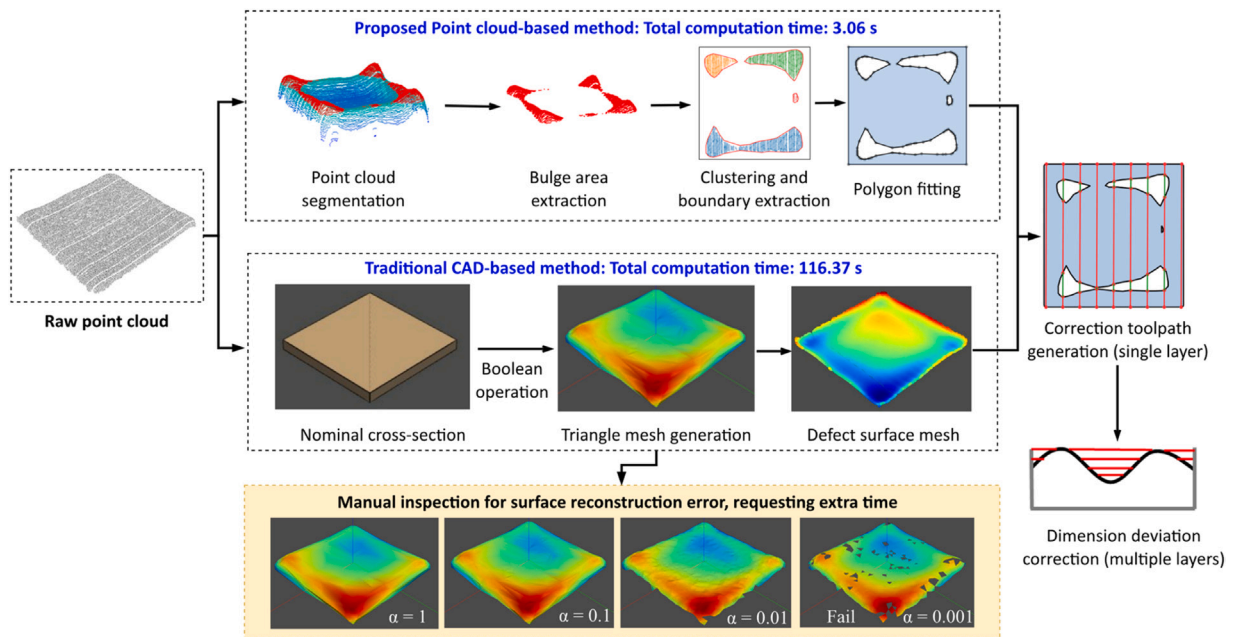


Fig. 20. Comparison between the proposed point cloud-based method and a traditional CAD-based method.

```

Input: List of points  $Q'(\mathbf{x}, \mathbf{y})$ ; tolerance  $\delta$ 
Output: An ordered list of points representing the computed concave polygon

Dataset after removing duplicated points:  $Q'(\mathbf{x}, \mathbf{y})$ 
IF Length( $Q'(\mathbf{x}, \mathbf{y})$ ) < 3:
    Return[null] # minimum 3 dissimilar points is required
ENDIF
Apply Delaunay triangulation and obtain: Triangle mesh  $\mathbf{Tri}(T) = \mathbf{DT}(Q(\mathbf{x}, \mathbf{y}))$ 
FOR triangle  $T$  in triangle mesh  $\mathbf{Tri}(T)$ :
    IF  $T \in$  outer boundary:
        FOR neighbour triangle  $T'$  on edge  $E'$  of  $T$ :
            IF no neighbour  $T'$  found:
                Add triangle edge  $E'$  from  $T$  to the Boundary vertices  $B(p)$ 
            ENDIF
            IF edge length  $E'$  in  $T >$  tolerance:
                Add edge  $E'$  into deletion list:  $D(e) = E' \cup D(e)$ 
            ENDIF
        ENDFOR
    WHILE  $D(e) \neq$  Empty:
        Edge  $E = \text{pop}(D(e))$ 
        # Triangle will not be deleted if it contains two boundary edges
        IF triangle  $T(E)$ .count(boundary edges) > 1:
            Continue
        #Triangle will not be deleted if inside node is already on the boundary
        of another triangle
        IF inside point  $P$  in triangle  $T(E) \in B(p)$ 
            Continue
        Remove  $E$  from  $B(p)$  #remove edge  $E$  from boundary list  $B(p)$ 
    ENDWHILE
Return  $B(p)$ 
    
```

Fig. A1. Concave hull algorithm for identifying concave boundary polygon of point cloud clusters.

```

Input: a single line element  $L_{input}$ ; a polygon  $Polygon\{E\}$  with exterior and interior boundary edges
Output: An ordered list of intersection points:  $Q'(p)$ ; laser-on segments:  $O(L)^{on}$ ; laser-off segments:  $O(L)^{off}$ 

 $Q(p) = \{\}$  # List of intersection point
FOR edge  $E'$  in  $Polygon\{E\}$ :
  IF  $E'$  intersects  $L_{input}$ :
    Intersection point:  $P' = E' \cap L_{input}$ 
    Append point  $P'$  to the list:  $Q(p) = P' \cup Q(p)$ 
  ENDIF
ENDFOR
Sort the  $Q(p)$  in ascending/descending order:  $Q'(p) = Sort(Q(p))$ 
FOR  $P'$  in  $Q'(p)$ :
  Current line segment:  $O' = P'P'^{+1}$ 
  Let point  $P$  be a point on  $O'$ :  $P \in P'P'^{+1}$ 
  IF  $P \in Polygon\{E\}$ :
    THEN  $O' \in Polygon\{E\}$ 
    Append current segment to laser-off segments:  $O(L)^{off} = O' \cup O(L)^{off}$ 
  ELSE
    Append current segment to laser-on segments:  $O(L)^{on} = O' \cup O(L)^{on}$ 
  ENDIF
ENDFOR

```

Fig. B1. Line-polygon intersection and segmentation algorithm.

tool-paths, which resulted in excessive laser irradiation and feeding of the powders. The measured surface at every cycle visualises the growth of the part during the fabrication. The dimensional deviation of the part accumulated and propagated, and the dimension deteriorated over time. As a result, the final part has severe geometric errors. Fig. 15(b) shows the part built with the in-process dimension correction strategy implemented. Dimensional deviations that occurred in the intermediate layers were corrected immediately and filled by the updated tool-path. As a result, the dimensional deviations were avoided. The part showed a uniform surface growth, and the final part could have a flat surface, as visualised in the measured surface at every cycle. To quantify the difference in dimensional accuracy between the corrected and the not corrected parts, the final dimensions of the two parts were compared with the ideal dimension, respectively. By integrating the absolute volume errors at each point, the total deviations are  $1767.6 \text{ mm}^3$  for the uncorrected part and  $334.1 \text{ mm}^3$  for the corrected part. It indicates that the dimensional accuracy of the corrected part was significantly improved by implementing the proposed correction strategy. It should be noted that the laser displacement sensor was exposed to various environmental influencing factors during the LAAM process. Due to harsh operating conditions, most of the influences on the sensors depend on the surface condition, such as powder particles spreading on the surface of the deposited part. Note that the quality of the profiling can also be affected by the light reflectivity. In addition, the accuracy of the sensor is linked with the motion accuracy and stability of the robot.

Fig. 16 shows the point cloud-based tool-path generation and dimension correction process for one layer when fabricating the part in Fig. 15(b). In Fig. 16(a), the original part at intermediate layer 16 (8 mm height) showed severe dimensional deviations. The point cloud of this intermediate surface was sliced by the reference plane. Subsequently, the correction tool-path was generated based on methodologies described in Section 4, as shown in Fig. 16(b). Fig. 16(c) shows the part after one layer of dimension correction.

In each cycle, the cross-sectional profiles in the XZ-plane were extracted from the point clouds and plotted in Fig. 17. Fig. 17(a) shows

the apparent unevenness of the surface profile for the first part without correction. The dimensional deviation propagated and accumulated as the build height increased. In contrast, Fig. 17(b) shows the flat surface profiles in the second part with dimension correction. Any dimensional deviations observed in the lower layers were compensated immediately by the correction tool-paths, and hence it did not deteriorate with the increase of build height.

#### 4.2. Cross-sectional morphology and hardness test

The subsurface microstructures of the as-deposited parts were investigated and compared. The cross-sections (in the XZ-plane) of the parts with and without dimension correction are presented in Fig. 18. The layer boundaries are highlighted by yellow dotted lines. As shown in Fig. 18(a), the part without correction contained significantly distorted layers. In comparison, in Fig. 18(b) where the proposed surface correction strategy was applied, relatively flat layer boundaries were observed.

Vickers hardness tests were conducted for both dimensionally corrected and uncorrected parts, resulting in four hardness profiles as plotted in Fig. 19. Hardness values were obtained along the edge and middle lines for each part, as illustrated in the top-left sub-figure of Fig. 19(b). Fig. 19(b) also shows the solidified melt pool traces formed by the correction tool-path along the edge line. It was observed that the variations of hardness were not significant after the dimension correction. This result was desirable because the objective of the proposed correction strategy was to improve the dimensional accuracy of the part without altering its mechanical properties.

#### 4.3. Comparison with traditional CAD-based surface reconstruction method

The proposed point cloud-based tool-path generation method is compared to a conventional CAD-based surface reconstruction method (Wilson et al., 2014) both qualitatively (in terms of procedural

differences) and quantitatively (in terms of computation time). The traditional CAD-based method, as shown in Fig. 20, includes steps such as triangular mesh creation, manual inspections for reconstruction errors, nominal cross-section extraction from the CAD model, and Boolean operation to produce mesh for the defects. The triangle mesh generation was based on a widely used alpha-shape algorithm (Edelsbrunner et al., 1983). In the alpha-shape algorithm, the parameter  $\alpha$  defines the degree of approximation, which has a substantial influence on the surface reconstruction results. A smaller  $\alpha$  value can result in a finer mesh, but it may cause surface reconstruction to fail. As a result, manual inspection is required to ensure successful surface reconstruction, which is inconvenient and time-consuming. Following this, the defects are obtained by calculating the Boolean difference between the nominal cross-section of the part and the reconstructed surface. Aside from the time spent on manual inspection, the total computing time for mesh generation and Boolean operation is approximately 116.47 s. On the contrary, the proposed method extracts dimension deviation boundaries directly from raw point cloud data, which takes only 3.06 s to generate a single layer correction toolpath. Therefore, the proposed method makes it feasible for on-machine and in-process toolpath generation for dimension deviation correction, eliminating the need for manual parameter tuning and inspections.

## 5. Conclusions

An effective solution to ensure the dimensional accuracy of the LAAM-fabricated part was presented in this paper. A laser displacement sensor was integrated into a robot-based LAAM system to perform on-machine laser scanning measurement. By using 3D point clouds as the feedback data, an in-process adaptive dimension correction strategy of the intermediate layers was proposed. The proposed strategy was composed of the cyclic steps for initial deposition, measurement, point cloud processing, and correction tool-path generation and execution. A dedicated software platform was developed to facilitate the dimension correction procedure. Surface defects that occurred in the intermediate layers can be detected and corrected immediately without human intervention. Experiments have shown that the dimensional accuracy of the manufactured part can be significantly improved by implementing the proposed correction strategy. It has also been verified through hardness tests that the mechanical properties would not be altered by the dimension correction. Future work will involve algorithms to automatically optimise the correction tool-path pattern and the number of measurements to improve the process efficiency while maintaining dimensional accuracy. More complex geometries with the varying cross-sectional area will be considered. Additionally, a subtractive machining process will be used if the surface distortions are too complicated to be corrected by AM.

## CRedit authorship contribution statement

**Peng Xu:** Methodology, Formal analysis, Validation, Investigation, Writing – original draft. **Xiling Yao:** Conceptualization, Methodology, Writing – review & editing. **Lequn Chen:** Software, Data Curation, Validation. **Chenyang Zhao:** Visualization. **Kui Liu:** Resources. **Seung Ki Moon:** Supervision. **Guijun Bi:** Resources, Writing – review & editing, Project administration, Funding acquisition.

## Declaration of Competing Interest

The authors declare that they have no known competing financial interests or personal relationships that could have appeared to influence the work reported in this paper.

## Acknowledgments

This work was supported by the Agency for Science, Technology and

Research (A\*STAR) of Singapore through the Industry Alignment Fund - Pre-positioning Programme (Grant No. A1893a0031), Career Development Fund, Singapore (Grant No. C210812030), Academy of Sciences Project of Guangdong Province (Grant No. 2016GDASRC-0105), Guangdong Basic and Applied Basic Research Foundation (Grant No. 2021A1515110043), National Natural Science Foundation of China (Grant No. 52005135), Stable Support Program for Shenzhen Higher Education Institutions (Grant No. GXWD20201230155427003-20200805182127001), and Shenzhen Science and Technology Program (Grant No. RCBS20200714114958150).

## Appendix A. : Concave hull algorithm

See appendix Fig. A1.

## Appendix B. : Line-polygon intersection and segmentation algorithm

See appendix Fig. B1.

## References

- Akbari, M., Kovacevic, R., 2019. Closed loop control of melt pool width in robotized laser powder-directed energy deposition process. *Int. J. Adv. Manuf. Technol.* 104, 2887–2898. <https://doi.org/10.1007/s00170-019-04195-y>.
- Asaedi, S., Didehvar, F., Mohades, A., 2017.  $\alpha$ -concave hull, a generalization of convex hull. *Theor. Comput. Sci.* 702, 48–59. <https://doi.org/10.1016/j.tcs.2017.08.014>.
- Chen, L., Yao, X., Xu, P., Moon, S.K., Bi, G., 2021. Rapid surface defect identification for additive manufacturing with in-situ point cloud processing and machine learning. *Virtual Phys. Prototyp.* 16, 50–67. <https://doi.org/10.1080/17452759.2020.1832695>.
- Chen, L., Yao, X., Xu, P., Moon, S.K., Bi, G., 2020. Surface Monitoring for Additive Manufacturing with in-situ Point Cloud Processing. In: 2020 6th International Conference on Control, Automation and Robotics (ICCAR). Presented at the 2020 6th International Conference on Control, Automation and Robotics (ICCAR), pp. 196–201. <https://doi.org/10.1109/ICCAR49639.2020.9108092>.
- Ding, D., Zhao, Z., Huang, R., Dai, C., Zhang, X., Xu, T., Fu, Y., 2021. Error modeling and path planning for freeform surfaces by laser triangulation on-machine measurement. *IEEE Trans. Instrum. Meas.* 70, 1–11. <https://doi.org/10.1109/TIM.2021.3063751>.
- Ding, Y., Warton, J., Kovacevic, R., 2016. Development of sensing and control system for robotized laser-based direct metal addition system. *Addit. Manuf.* 10, 24–35. <https://doi.org/10.1016/j.addma.2016.01.002>.
- Edelsbrunner, H., Kirkpatrick, D., Seidel, R., 1983. On the shape of a set of points in the plane. *IEEE Trans. Inf. Theory* 29, 551–559. <https://doi.org/10.1109/TIT.1983.1056714>.
- Ester, M., Kriegel, H.P., Sander, J., Xu, X., 1996. A density-based algorithm for discovering clusters in large spatial databases with noise. In: Proceedings of the Second International Conference on Knowledge Discovery and Data Mining, KDD'96, AAAI Press Portland, Oregon, pp. 226–231.
- Everton, S.K., Hirsch, M., Stravroulakis, P., Leach, R.K., Clare, A.T., 2016. Review of in-situ process monitoring and in-situ metrology for metal additive manufacturing. *Mater. Des.* 95, 431–445. <https://doi.org/10.1016/j.matdes.2016.01.099>.
- García-Díaz, A., Panadeiro, V., Lodeiro, B., Rodríguez-Araújo, J., Stavridis, J., Papacharalampopoulos, A., Stavropoulos, P., 2018. OpenLMD, an open source middleware and toolkit for laser-based additive manufacturing of large metal parts. *Robot. Comput. Integr. Manuf.* 53, 153–161. <https://doi.org/10.1016/j.rcim.2018.04.006>.
- Garmendia, I., Leunda, J., Pujana, J., Lamikiz, A., 2018. In-process height control during laser metal deposition based on structured light 3D scanning. *Procedia CIRP*, 19th CIRP Conference on Electro Physical and Chemical Machining, 23–27 April 2017, Bilbao, Spain 68, 375–380. <https://doi.org/10.1016/j.procir.2017.12.098>.
- Garmendia, I., Pujana, J., Lamikiz, A., Madarieta, M., Leunda, J., 2019. Structured light-based height control for laser metal deposition. *J. Manuf. Process.* 42, 20–27. <https://doi.org/10.1016/j.jmapro.2019.04.018>.
- Gibson, B.T., Bandari, Y.K., Richardson, B.S., Henry, W.C., Vetland, E.J., Sundermann, T. W., Love, L.J., 2020. Melt pool size control through multiple closed-loop modalities in laser-wire directed energy deposition of Ti-6Al-4V. *Addit. Manuf.* 32, 100993. <https://doi.org/10.1016/j.addma.2019.100993>.
- Guibas, L., Stolfi, J., 1985. Primitives for the manipulation of general subdivisions and the computation of Voronoi. *ACM Trans. Graph.* 4, 74–123. <https://doi.org/10.1145/282918.282923>.
- Han, X.-F., Jin, J.S., Wang, M.-J., Jiang, W., Gao, L., Xiao, L., 2017. A review of algorithms for filtering the 3D point cloud. *Signal Process.: Image Commun.* 57, 103–112. <https://doi.org/10.1016/j.image.2017.05.009>.
- He, P., Sun, C., Wang, Y., 2021. Material distortion in laser-based additive manufacturing of fuel cell component: Three-dimensional numerical analysis. *Addit. Manuf.* 46, 102188. <https://doi.org/10.1016/j.addma.2021.102188>.

- Hofman, J.T., Pathiraj, B., van Dijk, J., de Lange, D.F., Meijer, J., 2012. A camera based feedback control strategy for the laser cladding process. *J. Mater. Process. Technol.* 212, 2455–2462. <https://doi.org/10.1016/j.jmatprotec.2012.06.027>.
- Jafari, D., Vaneker, T.H.J., Gibson, I., 2021. Wire and arc additive manufacturing: Opportunities and challenges to control the quality and accuracy of manufactured parts. *Mater. Des.* 202, 109471 <https://doi.org/10.1016/j.matdes.2021.109471>.
- Kono, D., Yamaguchi, H., Oda, Y., Sakai, T., 2020. Stabilization of standoff distance by efficient and adaptive updating of layer height command in directed energy deposition. *CIRP J. Manuf. Sci. Technol.* 31, 244–250. <https://doi.org/10.1016/j.cirpj.2020.05.015>.
- Leach, R.K., Bourell, D., Carmignato, S., Donmez, A., Senin, N., Dewulf, W., 2019. Geometrical metrology for metal additive manufacturing. *CIRP Ann.* 68, 677–700. <https://doi.org/10.1016/j.cirp.2019.05.004>.
- Lee, D.T., Schachter, B.J., 1980. Two algorithms for constructing a Delaunay triangulation. *Int. J. Comput. Inf. Sci.* 9, 219–242. <https://doi.org/10.1007/BF00977785>.
- Li, M., Du, Z., Ma, X., Dong, W., Gao, Y., 2021. A robot hand-eye calibration method of line laser sensor based on 3D reconstruction. *Robot. Comput. -Integr. Manuf.* 71, 102136 <https://doi.org/10.1016/j.rcim.2021.102136>.
- Li, Xiao, Liu, B., Mei, X., Wang, W., Wang, X., Xun, Li, 2020. Development of an in-situ laser machining system using a three-dimensional galvanometer scanner. *Engineering* 6, 68–76. <https://doi.org/10.1016/j.eng.2019.07.024>.
- Lyu, J., Manoochehri, S., 2021. Online convolutional neural network-based anomaly detection and quality control for fused filament fabrication process. *Virtual Phys. Prototyp.* 16, 160–177. <https://doi.org/10.1080/17452759.2021.1905858>.
- Moreira, A., Santos, M.Y., 2007. Concave Hull: A k-Nearest Neighbours Approach for the Computation of the Region Occupied by a Set of Points. INSTICC Press.
- Schmidt, M., Merklein, M., Bourell, D., Dimitrov, D., Hausotte, T., Wegener, K., Overmeyer, L., Vollertsen, F., Levy, G.N., 2017. Laser based additive manufacturing in industry and academia. *CIRP Ann.* 66, 561–583. <https://doi.org/10.1016/j.cirp.2017.05.011>.
- Shi, T., Shi, J., Xia, Z., Lu, B., Shi, S., Fu, G., 2020. Precise control of variable-height laser metal deposition using a height memory strategy. *J. Manuf. Process.* 57, 222–232. <https://doi.org/10.1016/j.jmapro.2020.05.026>.
- Svetlizky, D., Das, M., Zheng, B., Vyatskikh, A.L., Bose, S., Bandyopadhyay, A., Schoenung, J.M., Lavernia, E.J., Eliaz, N., 2021. Directed energy deposition (DED) additive manufacturing: physical characteristics, defects, challenges and applications. *Mater. Today*. <https://doi.org/10.1016/j.mattod.2021.03.020>.
- Wilson, J.M., Piya, C., Shin, Y.C., Zhao, F., Ramani, K., 2014. Remanufacturing of turbine blades by laser direct deposition with its energy and environmental impact analysis. *J. Clean. Prod.* 80, 170–178. <https://doi.org/10.1016/j.jclepro.2014.05.084>.
- Zhou, Z., Shen, H., Liu, B., Du, W., Jin, J., Lin, J., 2022. Residual thermal stress prediction for continuous tool-paths in wire-arc additive manufacturing: a three-level data-driven method. *Virtual Phys. Prototyp.* 17, 105–124. <https://doi.org/10.1080/17452759.2021.1997259>.